Impact of SAR Image Resolution on Polarimetric Persistent Scatterer Interferometry With Amplitude Dispersion Optimization

Feng Zhao, *Member, IEEE*, Jordi J. Mallorqui, *Senior Member, IEEE*, and Juan M. Lopez-Sanchez, *Senior Member, IEEE*

***Abstract*— Polarimetric persistent scatterer interferometry (PolPSI) takes advantage of polarimetric optimization algorithms that enhance interferograms' phase quality by adequately combining the available polarization channels (e.g., HH, VV, HV, and VH) into an improved one. Amplitude dispersion (D_A) is one of the commonly used phase quality metrics for this optimization. The resolution of the images is supposed to have an impact on the performance of D_A-based PolPSI in terms of both pixel density and quality. In this research, this impact is investigated. Specifically, 30 quad-pol RADARSAT-2 images over Barcelona with a resolution around 5 m in both range and azimuth are employed to generate additional data sets with degraded resolutions, ranging from 7.5 to 20 m. The results confirm that, in all cases, the ability of D_A to select high-quality pixels, i.e., persistent scatterers, decreases when the spatial resolution worsens because the loss of resolution increases the number of scatterers present in a resolution cell. In addition, it would be expected that the performance of the polarimetric optimization of D_A would tend to decrease when the spatial resolution worsens. However, for all employed resolutions, the polarimetric optimization improves the density and quality of PSs with respect to that of any single polarimetric channel. Moreover, this improvement is more noticeable, in relative terms, as the image resolution degrades.**

***Index Terms*— Ground deformation, interferometric phase optimization, persistent scatterer interferometry (PSI), polarimetry, synthetic aperture radar (SAR) image resolution.**

I. Introduction

DUE to its high efficiency and millimeter accuracy of deformation monitoring, persistent scatterer interferometry (PSI) [1]–[8] with synthetic aperture radar (SAR) data has been routinely used in terrain and infrastructures displacement detection and monitoring. Despite its successful performance in monitoring ground deformations related to subsidence [9], landslides [10], earthquakes, and other geological environmental hazards [11], [12], in some areas, conventional PSI techniques may suffer from the lack of acceptable densities of coherent scatterers. In the areas, such as the vegetated ones, pixels may be affected by severe decorrelation [13], thus making their phases noisy and unqualified for PSI applications.

To improve the performance of conventional PSI techniques in these cases, two categories of algorithms have been proposed. On the one hand, SqueeSAR [14] and similar techniques [15]–[18] incorporate the use of distributed scatterers (DSs). These techniques usually start with the identification of homogeneous pixels (HPs), and then, DS pixels are filtered and optimized with their HPs to reduce the impact of decorrelation. Thus, both the quality and quantity of pixels for the PSI processing are increased due to this adaptive filtering, enabling the production of better deformation maps. On the other hand, according to the Polarimetric SAR Interferometry (PolInSAR) theory [19], [20], the observed targets respond differently to different polarizations. Hence, by searching for the optimum scattering responses for each pixel, its interferometric phase quality can be largely improved. As more and more satellites with the capability of acquiring polarimetric data have been deployed, it is possible to extend the PSI algorithms into the polarimetric domain. Under these circumstances, the polarimetric persistent scatterers interferometry SAR (PolPSI) has been proposed [21]–[32]. In PolPSI, two-phase quality criteria are commonly used for pixels' optimization. The first one is the coherence, which is well adapted for DS pixels' optimizations but entails an inevitable resolution loss. For deterministic or permanent scatterers (PS) candidate pixels' optimization, the dispersion of amplitude (D_A) criterion is usually employed. The former works with multilooked interferograms, and thus,

Manuscript received September 7, 2020; revised December 8, 2020 and January 18, 2021; accepted February 4, 2021. This work was supported in part by the Spanish Ministry of Economy, Industry and Competitiveness (MINECO), the State Research Agency (AEI) and the European Funds for Regional Development (EFRD) under Project TEC2017-85244-C2-1-P and Project TEC2017-85244-C2-2-P, in part by the National Natural Science Foundation of China under Grant 42004011 and Grant 41874044, in part by the China Postdoctoral Science Foundation under Grant 2020M671646, in part by the Priority Academic Program Development (PAPD) of Jiangsu Higher Education Institutions (Science and Technology of Surveying and Mapping), and in part by the CommSensLab, which is Unidad de Excelencia Maria de Maeztu MDM-2016-0600 financed by the AEI, Spain. *(Corresponding author: Jordi J. Mallorqui.)*

Feng Zhao was with CommSensLab, Universitat Politècnica de Catalunya, 08034 Barcelona, Spain. He is now with the School of Environment Science and Spatial Informatics, China University of Mining and Technology (CUMT), Xuzhou 221116, China, and also with the Key Laboratory of Land Environment and Disaster Monitoring of the Ministry of Natural Resources of China, Xuzhou 221116, China (e-mail: feng.zhao@cumt.edu.cn).

Jordi J. Mallorqui is with CommSensLab, Universitat Politècnica de Catalunya, 08034 Barcelona, Spain (e-mail: mallorqui@tsc.upc.edu).

Juan M. Lopez-Sanchez is with the Signals, Systems and Telecommunications Group, Institute for Computer Research (IUII), Universitat d'Alacant, 03080 Alicante, Spain (e-mail: juanma.lopez@ua.es).

Color versions of one or more figures in this article are available at https://doi.org/10.1109/TGRS.2021.3059247.

Digital Object Identifier 10.1109/TGRS.2021.3059247

the resolution is worsened, while the latter works at the original resolution of the SAR images.

PolPSI techniques improve the phase quality of SAR pixels by searching for their optimal scattering response from the point of view of the optimization criterion. The more the scattering mechanisms (SM) present within a resolution cell, the more difficult to find the optimum response. As the resolution worsens, SAR pixels are more likely to contain more diverse SM; thus, it can be anticipated that pixels' resolution may have a significant influence on the performance of PolPSI optimization techniques. However, to the best of our knowledge, this issue has not been investigated in detail. In this article, the impact of SAR image resolution on the PolPSI optimization with D_A is investigated. The study has been done based on five quad-pol SAR data sets. From the original one, with a resolution around 5 m $\times$ 5 m, four others have been generated with degraded resolutions up to 20 m $\times$ 20 m.

The main novelty of this article is twofold. On the one hand, the performance of the PolPSI algorithm as a function of SAR images' resolution has not been evaluated previously in the literature, and as it will be shown later in the manuscript, the corresponding findings are not as expected. On the other hand, as the results will demonstrate, the improvement provided by PolPSI is also evident with dual-pol data (e.g. VV + VH, 20-m resolution). Therefore, PolPSI is perfectly applicable to dual-pol data sets, such as the ones from Sentinel-1, for which there is no swath reduction due to the polarimetric acquisition mode (i.e. it only happens in the quad-pol case).

This article is organized as follows. In Sections II and III, the principles of D_A-based PolPSI and the available data set are introduced. Section IV describes the results obtained. Finally, the conclusions are presented in Section V.

II. Polarimetric Persistent Scatterer Interferometry With D_A Optimization

The PolPSI algorithm with D_A optimization consists of two main procedures: interferograms optimization (whose flowchart is shown in Fig. 1) and PSI processing. The coherent pixels technique (CPT) is employed for the PSI processing. A detailed description of CPT can be found in [3] and [5]. As this research is focused on the polarimetric optimization part, it will be introduced in this section.

PolInSAR requires two polarimetric SAR images acquired from two spatially or temporally separated locations [19], [25]. For one quad-pol PolSAR image, under the assumption of reciprocity, its scattering vector under the Pauli basis can be expressed as

$$\boldsymbol{k} = \frac{1}{\sqrt{2}}[S_{\mathrm{hh}} + S_{\mathrm{vv}},\ S_{\mathrm{hh}} - S_{\mathrm{vv}},\ 2S_{\mathrm{hv}}]^T \tag{1}$$

where S_{hh} and S_{vv} are the horizontal and vertical copolar channels and S_{vh} the cross-polar channel of the PolSAR image's scattering matrix, respectively. If the PolSAR image is dual-pol and only the copolar channels are available, (1) changes to

$$\boldsymbol{k} = \frac{1}{\sqrt{2}}[S_{\mathrm{hh}} + S_{\mathrm{vv}},\ S_{\mathrm{hh}} - S_{\mathrm{vv}}]^T \tag{2}$$

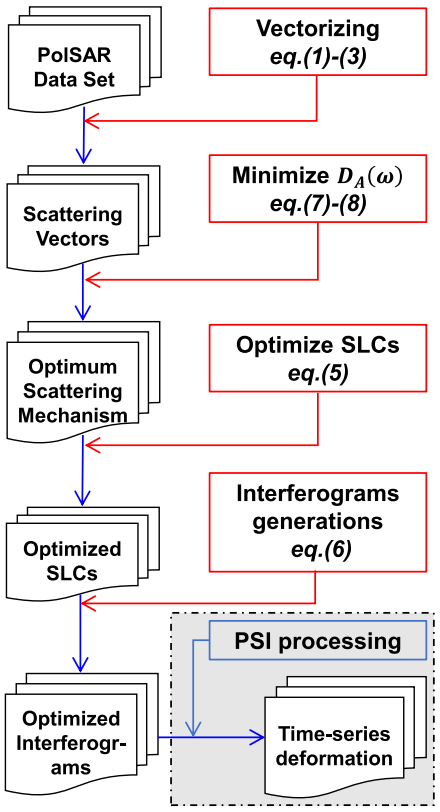

Fig. 1. Flowchart of the polarimetric persistent scatterer interferometry (PolPSI) with D_A optimization.

or (3) in case the cross-polar channel and one of the two copolar channels (denoted as xx) are available

$$\boldsymbol{k} = [S_{\mathrm{xx}},\ 2S_{\mathrm{hv}}]^T. \tag{3}$$

Then, based on the scattering vectors obtained through (1)–(3), the PolInSAR vector can be defined as

$$\boldsymbol{K} = [\boldsymbol{k}_1,\ \boldsymbol{k}_2]^T \tag{4}$$

where $\boldsymbol{k}_1$ and $\boldsymbol{k}_2$ are the two scattering vectors from the primary and secondary PolSAR images that form the interferometric pair. Each polarimetric channel would generate a different interferogram. A single interferogram can be synthesized based on $\boldsymbol{K}$ with two normalized complex projection vectors $\boldsymbol{\omega}_1$ and $\boldsymbol{\omega}_2$, which are usually regarded as SM, that combine for each image all available polarimetric channels into a single one [19], [20]. The two original scattering vectors $\boldsymbol{k}_1$ and $\boldsymbol{k}_2$ are projected onto the resulting SM with

$$\mu_i = \boldsymbol{\omega_i}^{\dagger} \cdot \boldsymbol{k}_i,\quad i = 1, 2 \tag{5}$$

where $\dagger$ refers to the conjugate transpose, and μ_1 and μ_2 are two scalar scattering coefficients, analogous to single-polarization SAR images [19], [20]. To avoid introducing artificial changes along time in the phase centers of the scatterers in PolPSI applications, $\boldsymbol{\omega}_1$ and $\boldsymbol{\omega}_2$ are forced to be identical, i.e., a single projection vector $\boldsymbol{\omega}$ is employed for all interferograms of the data set [19], [24], [25]. This condition is called equal SM (ESM) [33].

TABLE I
KEY PARAMETERS OF THE EMPLOYED POLSAR DATA SET

Sensor	Radarsat-2
Orbit	Descending
Acquisition mode	Stripmap
Polarization	Quad-pol
Nominal incidence angle	28° (near range) to 29.8° (far range)
Nominal pixel dimensions	5.1 × 4.7 m
Wavelength	5.55 cm
Number of interferograms	76
Average temporal baseline	68.5 day
Average spatial baseline	104.1 m

For deterministic scatterers, $\boldsymbol{k}_i$ in (5) corresponds to a deterministic vector [24], [25]. The expression for the vector interferogram can be obtained as [19]

$$I = \mu_1 \cdot \mu_2^* \tag{6}$$

where * is the complex conjugate. The pixel phase quality criterion D_A can be then expressed as

$$D_A = \frac{\sigma_A}{m_A} = \frac{1}{\overline{|\boldsymbol{\omega}^\dagger \boldsymbol{k}|}} \sqrt{\frac{1}{N}\sum_{i=1}^{N}\left(|\boldsymbol{\omega}^\dagger \boldsymbol{k}_i| - \overline{|\boldsymbol{\omega}^\dagger \boldsymbol{k}|}\right)^2} \tag{7}$$

with

$$\overline{|\boldsymbol{\omega}^\dagger \boldsymbol{k}|} = \frac{1}{N}\sum_{i=1}^{N}|\boldsymbol{\omega}^\dagger \boldsymbol{k}_i| \tag{8}$$

where σ_A and m_A are the standard deviation and mean of the images' amplitudes, N is the number of images, and the overline indicates the empirical mean value [24], [25].

The polarimetric optimization finds, for each pixel, $\boldsymbol{\omega}$ that minimizes its D_A. An exhaustive search of the polarimetric space, also known as Exhaustive Search Polarimetric Optimization (ESPO) method [24], has been used in this research because it provides the best performance in interferometric phase optimization among all possible methods. After the polarimetric optimization, through (5), the optimized SAR images are obtained. Then, the PSI processing can be carried out using the same PSI algorithms as for the single-pol case.

III. DATA SET

The data set is formed by 30 stripmap quad-pol Radarsat-2 images with a resolution of around 5 m × 5 m, which were acquired from May 2010 to July 2012 over the city of Barcelona. A section of the images that cover most of the city and the airport, with a size of 1602 × 4402 pixels, is selected as the study area. The key parameters of the data set are listed in Table I.

Additional data sets with coarser resolutions are generated from this original set of images. In order to simulate the acquisitions from a sensor with lower resolution, downsampling has been carried out in the spectral domain. Fig. 2 shows the process, which is almost identical for range and azimuth dimensions. The original spectrum, in any of the two dimensions, is unweighted to obtain an almost flat spectrum. Depending on the resolution reduction factor, which sets the new bandwidth, a rectangular window is applied to eliminate the frequencies beyond the new sampling frequency. Finally, the spectrum is weighted with the original window scaled to the new bandwidth. In practice, the last two steps are

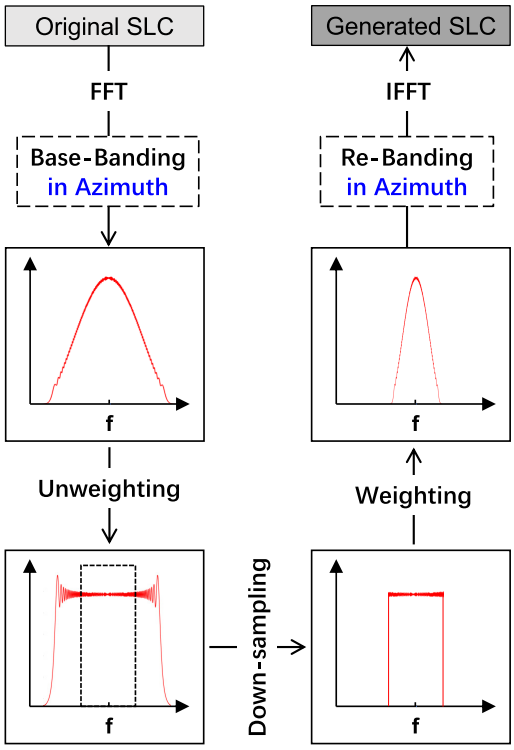

Fig. 2. Flowchart of the generation of the reduced resolution SLC SAR images. It is worth to be noted that the shift to baseband and back has to be done only in the azimuth dimension.

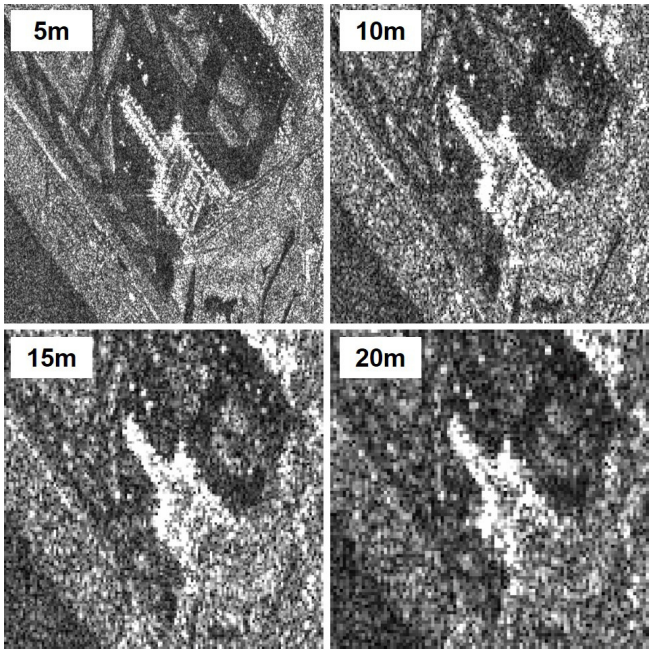

Fig. 3. SLC SAR amplitude images of the HH channel with different spatial resolutions over the Barcelona airport Terminal-1. The original SLC (with 5-m resolution) was acquired on May 5, 2010.

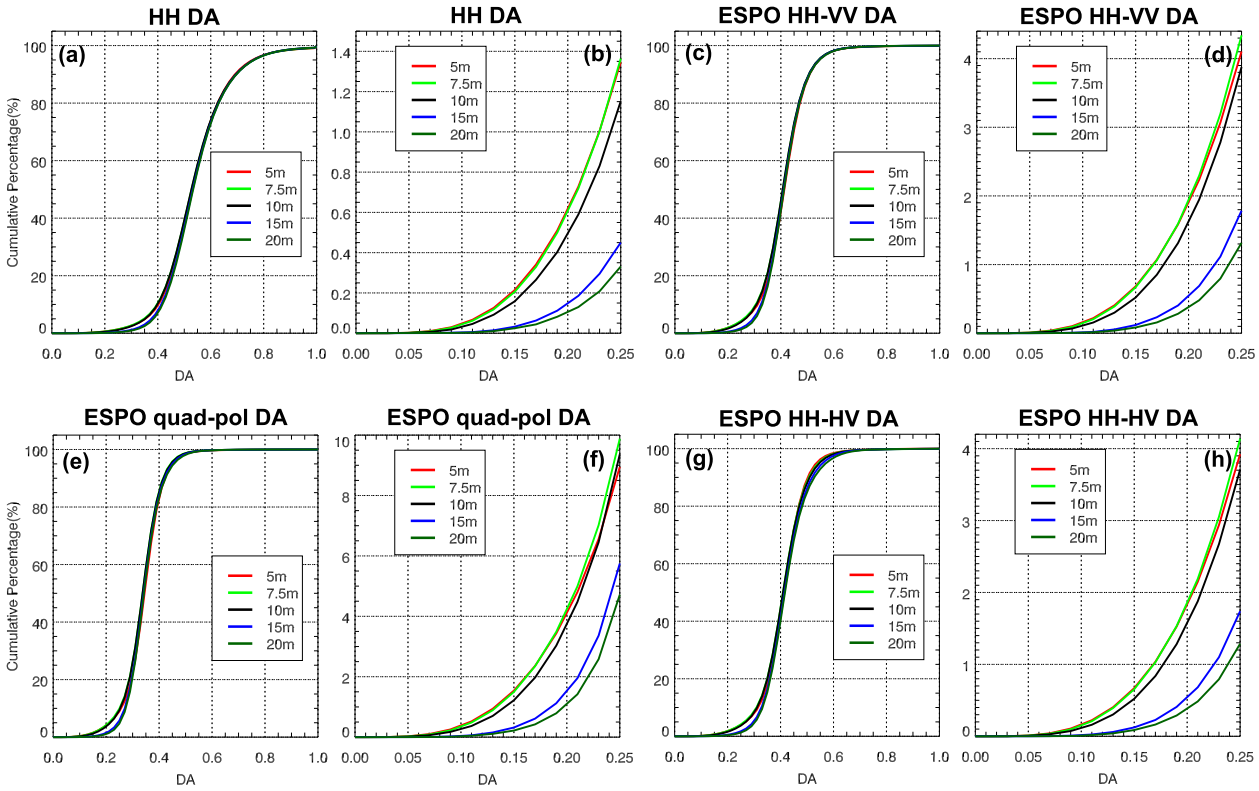

Fig. 4. (a), (c), (e), and (g) Histogram of D_A cumulative percentage derived by HH, ESPO HH+VV, ESPO quad-pol, and ESPO HH+HV polarimetric channels, respectively. (b), (d), (f), and (h) Detailed zoom of (a), (c), (e), and (g) for D_A values from 0 to 0.25. It should be noted that the vertical axis is different for each zoomed plot [i.e., (b), (d), (f), and (h)].

computed at the same time. In the azimuth dimension, there are two extra steps. In the beginning, the image is shifted to baseband as a function of the range-dependent Doppler centroid of the acquisition. After the resolution reduction, the final image is shifted back to its original Doppler centroid. Image parameters and orbital information are updated according to the new image bandwidths and sampling. Each new set of images is processed as if the images came from a real sensor. Therefore, a total of four new quad-pol data sets have been generated with resolutions around 7.5 m $\times$ 7.5 m, 10 m $\times$ 10 m, 15 m $\times$ 15 m, and 20 m $\times$ 20 m, respectively.

The amplitude of the HH channel of the first original SLC image (acquired on May 5, 2010) and the reduced resolution ones over the area of the Barcelona airport Terminal-1 are shown in Fig. 3. It can be observed that, when the resolution is progressively degraded, details start to disappear. For instance, the terminals' structures and edges of the runways can be well recognized in the 5-m resolution amplitude image, while these details can be hardly seen in the 20-m resolution one.

IV. Results and Analysis

A. Results of the D_A Optimization

The cumulative histograms of D_A for HH and for the optimizations provided with different combinations of input polarimetric channels are depicted in Fig. 4 at all the spatial resolutions considered. It is worth mentioning that the results corresponding to the VV+HV polarimetric combination are very similar to those of the HH+HV case; thus, they are not presented. As shown in Fig. 4, for all resolutions, the percentage of pixels with D_A below 0.4 is around 10%, 40%, and 80% for the HH channel [see Fig. 4(a)], the optimized dual-pol cases [see Fig. 4(c) and (g)], and the optimized quad-pol case [see Fig. 4(e)], respectively. This indicates that the polarimetric optimization improves the overall phase quality for all input data sets and all resolutions. As expected, the quad-pol data set performs much better than the dual-pol ones in the study area.

For all input polarimetric combinations, the percentage of th highest quality pixels (i.e., pixels with D_A less than 0.25) decreases as the images' resolution worsens. However, and surprisingly, the relative improvement in the quality of the pixels with respect to the HH channel increases as the resolution worsens. For instance, the improvement achieved with the quad-pol data with respect to HH is around 641%, 1,144%, and 1,293% for the data sets with resolutions of 5, 15, and 20 m, respectively.

The impact of SAR images' resolution on the performance of the D_A-based polarimetric optimization is the result of the combination of two main factors. In the first place, with the enlargement of the spatial resolution, each resolution cell has more chances to contain a higher number of significant scatterers with diverse SM, and therefore, a particular pixel is more unlikely to behave as a persistent scatterer. The significant decrease in the percentage of pixels with $D_A < 0.25$ (see Fig. 4) in the single-channel case when the resolution

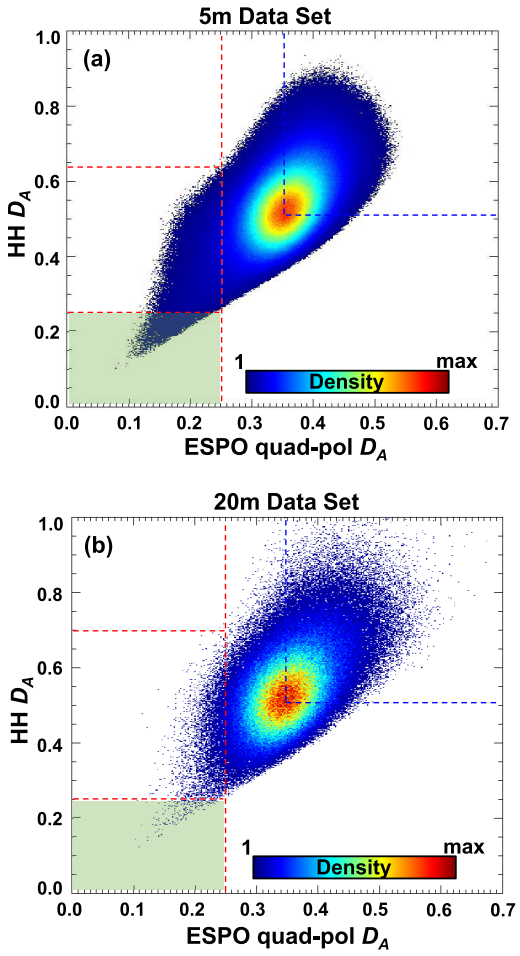

Fig. 5. Scatter plots between D_A at the HH channel and D_A with quad-pol data after ESPO optimization for (a) 5- and (b) 20-m resolution data sets.

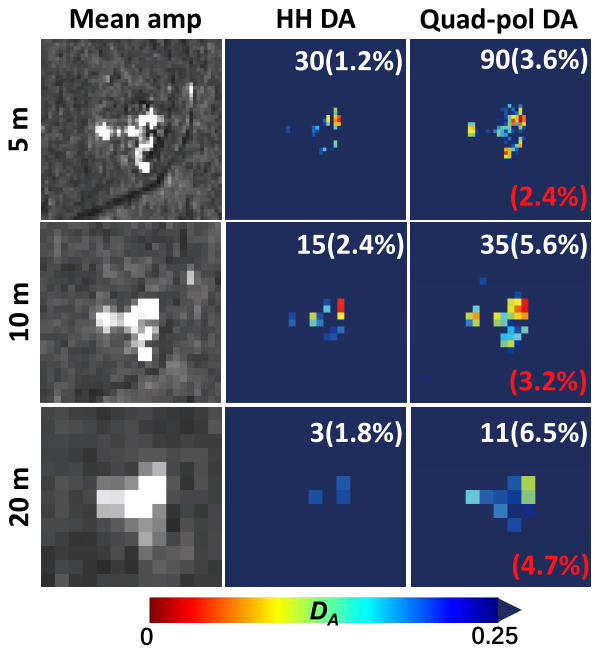

Fig. 6. Temporal mean amplitude and D_A (HH channel and quad-pol optimized) images over a navigation tower for 5-, 10-, and 20-m resolutions, respectively. The white value and percentage in the up-right corner denote the number and percentage of pixels with $D_A < 0.25$ (high-quality pixels), respectively. The red percentage in the down-right corner indicates the quad-pol data optimization achieved an improvement of high-quality pixels with respect to that of the HH channel.

worsens from 10 to 20 m strongly suggests that, in second place, the presence of the diverse SM in a pixel increases the chances of optimizing their amplitude dispersion with polarimetric optimization tools. In other words, in the image, there will be a higher percentage of pixels with mixed SM that can be benefited from the polarimetric optimization.

The scatter plots comparing D_A from the HH channel and after using ESPO with quad-pol SAR images for the 5- and 20-m data sets are shown in Fig. 5. It is worth mentioning that, to be comparable with the 20-m resolution data set, the D_A density values (i.e., the number of pixels with D_A values located in the plot bin) for the 5-m case have been divided by 16 (i.e., the resolution widening factor when generating the 20-m data set).

For the 5-m resolution data set, pixels with a quad-pol optimized D_A below 0.25 show values of D_A up to 0.65 at the HH channel; while, for the 20-m resolution data set, the counterpart is up to 0.7, as shown in Fig. 5. This indicates that, with the degradation of images' resolution, a larger range of pixels can be benefited by the polarimetric optimization. At the same time, as the green rectangles in Fig. 5 highlight, the percentage of pixels with D_A below 0.25 decreases with the enlargement of images' resolution regardless of the polarimetric optimization. Meanwhile, the centers of the two scatter plots (i.e., where the highest density bins are located) are very close to each other, but the distribution of the plot bins is more concentrated for the 5-m resolution case than for the 20-m one. This is due to the fact that pixels are more unlikely to behave as deterministic scatterers when their spatial resolution worsens.

To further demonstrate the above points, the image of D_A for HH and the quad-pol optimized channel and the temporal average amplitude for the three different resolutions around the navigation tower of the Barcelona airport is shown in Fig. 6. The value and percentage in the up-right corner of the images denote the number and percentage of pixels with $D_A < 0.25$, respectively. After the polarimetric optimization, for all the three cases, the final number of high-quality PSs has increased with respect to HH, and this improvement (as the red percentage in the down-right corner indicates) is more significant for the lower resolution cases. However, the best values of D_A for the 5-, 10-, and 20-m data sets are 0.0403, 0.0612, and 0.1395, respectively. These minimum values increase as the SAR image resolution worsens, which is due to the incapacity of a resolution cell to behave as a deterministic scatterer when there are many elements within it. In fact, a resolution cell formed by many deterministic scatterers does not behave as a deterministic scatterer since their relative positions change the radar response as a function of incidence angle and baseline. For instance, if they were distributed in a plane inside the resolution cell, there would be baseline decorrelation since the response of the whole cell would not correspond to a single point scatterer anymore.

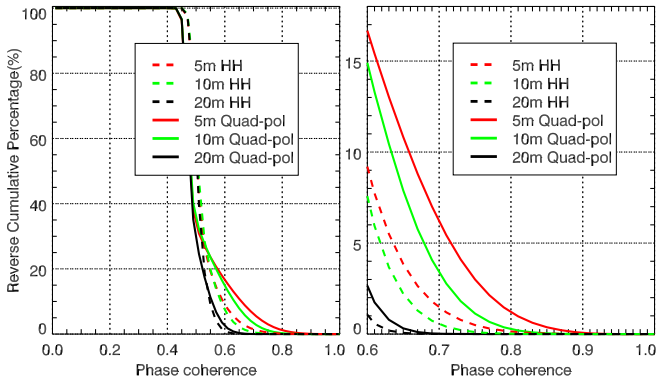

Fig. 7. (a) Reverse cumulative percentage of the temporal mean phase coherence of HH and quad-pol optimized for 5-, 10-, and 20-m resolutions. (b) Details of (a) for phase coherence from 0.6 to 1.0.

B. Analysis of the Temporal Mean of Phase Coherence

The temporal mean of the phase coherence, $\overline{\gamma_{\rm ph}}$, is also employed to study the impact of resolution on the performance of the D_A-based polarimetric optimization. $\overline{\gamma_{\rm ph}}$ is another phase quality estimator that corresponds to the local correlation computed only from interferometric phase values. $\overline{\gamma_{\rm ph}}$ ranges from 0 to 1, and higher values indicate a better interferometric phase quality [34]. The calculation of $\overline{\gamma_{\rm ph}}$ is obtained using

$$\overline{\gamma_{\rm ph}} = \frac{1}{N}\sum_{i=1}^{N}\gamma_{\rm ph} \tag{9}$$

with

$$\gamma_{\rm ph} = \frac{1}{M}\sqrt{\sum_{m=0}^{M-1}\cos^2(\phi_m) + \sum_{m=0}^{M-1}\sin^2(\phi_m)} \tag{10}$$

where N is the number of interferograms, and $\gamma_{\rm ph}$ is the phase coherence of one interferogram. M and ϕ_m are the number of averaged pixels in the estimation window and the interferometric phase, respectively [34].

The values of $\overline{\gamma_{\rm ph}}$ for the HH channel and the quad-pol optimized one for the three different resolutions have been computed, and they are shown in Fig. 7 and Table II. The conclusions are coincident with those obtained from the D_A results in the previous section. The phase quality has been improved via the polarimetric optimization for all resolution cases. The improvement achieved by the polarimetric optimization with respect to the HH channel is more significant for the coarse resolution data sets, as it can be seen in Table II. However, the percentage of high-quality pixels, those with optimized $\overline{\gamma_{\rm ph}}$ greater than 0.65, decreases from 10.8% to 0.31% as the images' resolution worsens.

C. Deformation Estimation Result

Finally, pixels with D_A less than 0.25 are selected as high-quality pixels for the PSI processing for all polarimetric combinations and for the different resolutions considered. Ground deformation estimation is carried out with SUBSIDENCE-GUI, the PSI processing chain of Universitat Politècnica de Catalunya (UPC) that implements the Coherent Pixels Technique (CPT) [5].

TABLE II
PERCENTAGE OF PIXELS WITH HIGH TEMPORAL MEAN PHASE COHERENCE

Pol. / Res.	Quad-pol	HH	Impro.	Quad-pol	HH	Impro.
$\overline{\gamma_{ph}}$	$\overline{\gamma_{ph}} \geq 0.60$			$\overline{\gamma_{ph}} \geq 0.65$		
5m	16.8%	9.2%	82%	10.8%	3.8%	184%
10m	14.9%	7.6%	96%	7.9%	2.2%	259%
20m	2.6%	1.1%	136%	0.31%	0.064%	384%

'Res.' and 'Pol.' are the abbreviations of 'Resolution' and 'Polarimetric channel', respectively. The Impro. columns are the improvements obtained by the full-pol approach w.r.t. the HH channel.

The estimated ground deformation over Barcelona retrieved from the HH channel and from the optimized quad-pol data with three different spatial resolutions is shown in Fig. 8. Despite the differences in the final PS pixel density, the ground deformation patterns obtained from the different approaches and data sets are in good agreement with each other. In addition, these results are also in good accordance with those of previous studies [24]–[26], which validates the correctness of the deformation maps.

The numbers of valid PSs in the estimated ground deformation results with all the data sets are listed in Table III. The detailed results support previous conclusions. The highest densities of pixels are obtained with high-resolution optimized quad-pol data, but, in all cases, the optimization is able to increase the number of selected pixels. In addition, the highest improvements in percentage relative to the HH channel are achieved with the lowest resolution data.

Time-series deformations derived from different approaches at a selected pixel, which is indicated in Fig. 8(e) by the yellow arrow and black circle, are shown in Fig. 9. Both the HH and quad-pol data obtained very similar time-series deformations. However, the results are different when comparing 5 and 20 m. This is mainly due to the different targets observed inside the resolution cell when resolution worsens from 5 to 20 m. For the 10-m resolution case, time-series deformations from the quad-pol and HH data are different. Specifically, the quad-pol time-series deformation is very similar to that of the 5-m data, whereas the HH result is close to that of 20-m resolution. The reasons could be that, on the one hand, the 10-m HH data tend to observe deformations of similar targets as the 20-m data; on the other hand, through the D_A-based polarimetric optimization, the 10-m quad-pol data are able to obtain the dominant SM, which is close to one of the 5-m data within the selected pixel. The Google Earth image over the selected pixel is presented in Fig. 9(d). As this optical image shows, many strong deterministic scatterers are located around the selected pixel, indicating that there is a high probability that different SMs are mixed in this pixel with the worsening of its resolution.

Better performance of PolPSI (with quad-pol data) compared with PSI (with HH data) in terms of atmospheric effect reduction is not easily observed from the time-series deformations in Fig. 9. This is because the atmospheric effects

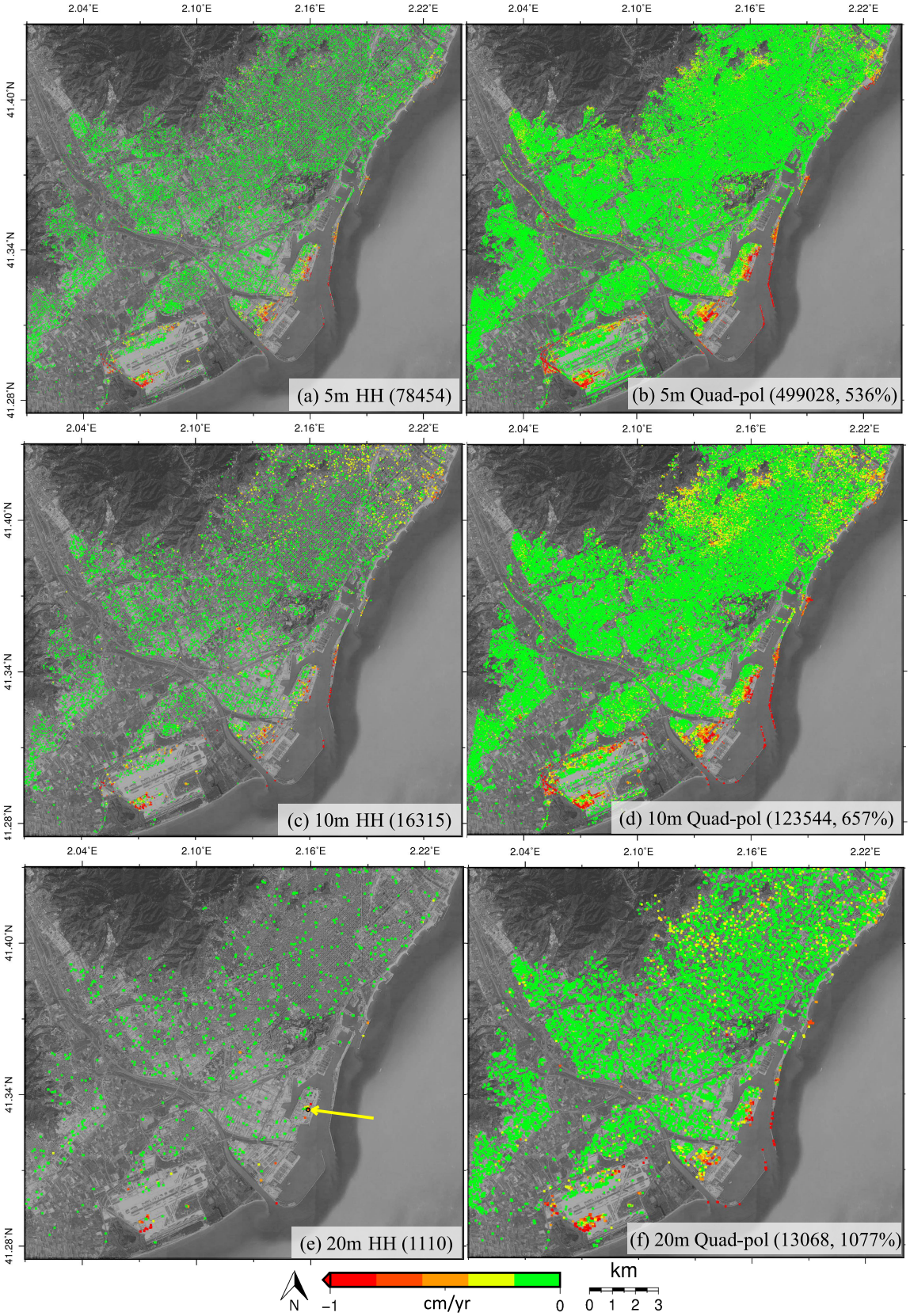

Fig. 8. Ground deformation velocity estimated with 5 m (top), 10 m (middle), and 20 m (bottom) resolution data sets, respectively. Results derived from (a), (c), and (e) HH channel and (b), (d), and (f) optimized quad-pol data. The number in brackets represents the final number of PS pixels obtained by each approach, and the improvement percentage is obtained by taking the HH channel as a reference for each resolution case.

TABLE III

NUMBER OF PSS OBTAINED BY USING D_A-BASED APPROACHES WITH DIFFERENT POLARIMETRIC COMBINATIONS OVER THE FIVE DIFFERENT RESOLUTION DATA SETS

Pol. / Res.	HH	Quad-pol	HH+VV	HH+HV	VV+HV
5m	99.5% / 78454 (0%)	96.7% / 499028 (536%)	99.4% / 239363 (205%)	99.4% / 229955 (193%)	99.5% / 231322 (195%)
7.5m	99.5% / 34841 (0%)	96.3% / 236578 (579%)	99.2% / 110781 (218%)	99.3% / 106404 (205%)	99.3% / 104834 (201%)
10m	99.7% / 16315 (0%)	95.9% / 123544 (657%)	99.0% / 54631 (239%)	99.2% / 52818 (224%)	99.2% / 51194 (214%)
15m	99.3% / 2704 (0%)	92.2% / 30015 (1010%)	98.5% / 10392 (284%)	99.0% / 10391 (284%)	98.7% / 9817 (263%)
20m	99.4% / 1110 (0%)	90.2% / 13068 (1077%)	98.8% / 4248 (283%)	98.5% / 4260 (284%)	98.7% / 4006 (261%)

'Res.' and 'Pol.' are the abbreviations of 'Resolution' and 'Polarimetric channel', respectively. "i% / N (j%)" in the table represent the viability (i%) of PS candidates after PSI processing, the final number of PSs (N) and its increase (j%) w.r.t. that of the single HH polarimetric approach. The viability here means the percentage of final valid PS over the initial PS candidates.

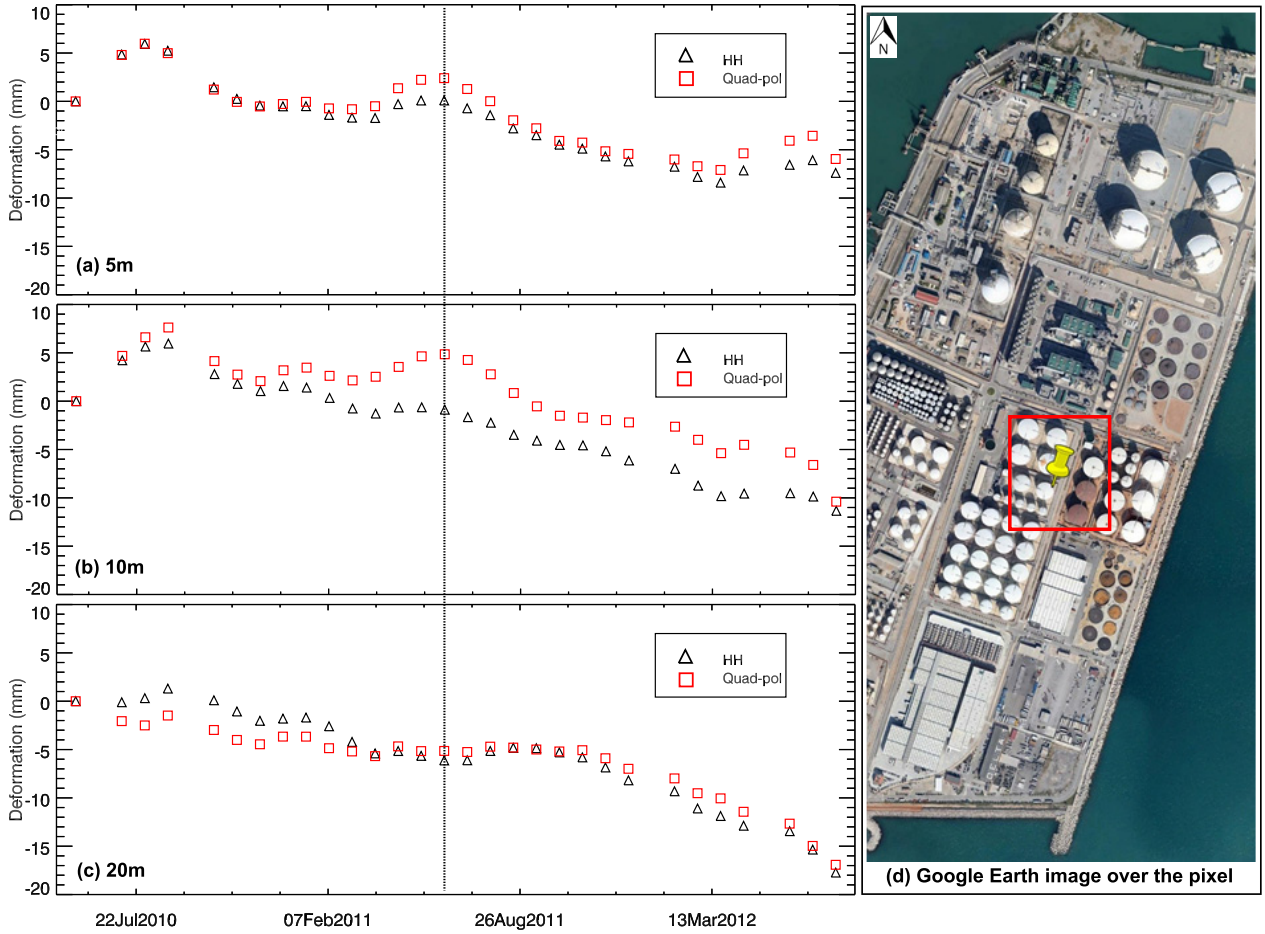

Fig. 9. Time-series deformations of a selected pixel derived from (a) 5-, (b) 10-, and (c) 20-m resolution data sets, respectively. The location of the selected pixel is indicated in Fig. 8(e) by the yellow arrow and black circle. The Google Earth image over the selected pixel is shown in (d), where the red rectangle and yellow pin indicate the pixel's location.

on InSAR in the study area are not too strong. However, the higher the increase in high-quality pixel density obtained by PolPSI, the better the reduction of the atmospheric effects on the deformation time series. This is because atmospheric phases are usually assumed to be spatially correlated and temporally uncorrelated, so they are estimated through spatial low-pass and temporal high-pass filters. A higher density of qualified pixels can contribute to a better performance of the spatial low-pass filter, resulting in better atmospheric phase estimations. Given the negligible atmospheric effects in the deformation time series, this issue has not been explicitly investigated in this work, and it is left for future research.

V. CONCLUSION

The impact of the spatial resolution of SAR images on the polarimetric optimization of D_A for PSI processing has been investigated. From an original Radarsat-2 quad-pol data set with a resolution around 5 m in both range and azimuth, four additional sets have been derived with decreasing resolutions:

7.5, 10, 15, and 20 m. The tests carried out have allowed us to obtain the following main conclusions.

1) The D_A-based polarimetric optimization improves the density of valid PS pixels with respect to a single-pol reference channel for any input PolSAR data set, either dual- or quad-pol, and with any resolution ranging from 5 to 20 m.
2) The improvement in the density of valid PSs is more significant in percentage with respect to the reference channel as the image resolution worsens. Therefore, PolSAR data sets with the coarse resolution are more benefited from the polarimetric optimization than fine resolution ones.
3) When the image resolution worsens, the best values of D_A for individual pixels are worse (i.e. higher), independently of the polarimetric optimization, since there are more elements in the resolution cell, and consequently, they behave more differently compared with deterministic scatterers than when there are fewer elements.

From this study, it can be also concluded that it is worth processing the two channels (i.e, VV and VH) of the Sentinel-1 data by applying the polarimetric optimization with D_A for PSI applications since it will provide more density of PSs than using just the VV channel (which is the common practice). Being a standard dual-pol mode, with a common transmitted polarization and two receiving ones, there is no drawback in swath reduction with respect to single-pol data (contrarily to what would happen with a quad-pol system).

ACKNOWLEDGMENT

Radarsat-2 images were provided by MDA in the framework of the scientific project SOAR-EU 6779. The DEMs were from the Instituto Geografico Nacional of Spain. Some figures were prepared using the public domain GMT software (Wessel and Smith, 1998). Optical images are provided by Google Earth.

REFERENCES

[1] A. Ferretti, C. Prati, and F. Rocca, "Permanent scatterers in SAR interferometry," *IEEE Trans. Geosci. Remote Sens.*, vol. 39, no. 1, pp. 8–20, 2001.
[2] P. Berardino, G. Fornaro, R. Lanari, and E. Sansosti, "A new algorithm for surface deformation monitoring based on small baseline differential SAR interferograms," *IEEE Trans. Geosci. Remote Sens.*, vol. 40, no. 11, pp. 2375–2383, Nov. 2002.
[3] O. Mora, J. J. Mallorqui, and A. Broquetas, "Linear and nonlinear terrain deformation maps from a reduced set of interferometric SAR images," *IEEE Trans. Geosci. Remote Sens.*, vol. 41, no. 10, pp. 2243–2253, Oct. 2003.
[4] A. Hooper, P. Segall, and H. Zebker, "Persistent scatterer interferometric synthetic aperture radar for crustal deformation analysis, with application to Volcán alcedo, Galápagos," *J. Geophys. Res.*, vol. 112, no. B7, 2007.
[5] P. Blanco-Sánchez, J. J. Mallorquí, S. Duque, and D. Monells, "The coherent pixels technique (CPT): An advanced DInSAR technique for nonlinear deformation monitoring," *Pure Appl. Geophys.*, vol. 165, no. 6, pp. 1167–1193, Jun. 2008.
[6] R. Iglesias, J. J. Mallorqui, and P. Lopez-Dekker, "DInSAR pixel selection based on sublook spectral correlation along time," *IEEE Trans. Geosci. Remote Sens.*, vol. 52, no. 7, pp. 3788–3799, Jul. 2014.
[7] F. Zhao and J. J. Mallorqui, "A temporal phase coherence estimation algorithm and its application on DInSAR pixel selection," *IEEE Trans. Geosci. Remote Sens.*, vol. 57, no. 11, pp. 8350–8361, Nov. 2019.
[8] R. Iglesias *et al.*, "PSI deformation map retrieval by means of temporal sublook coherence on reduced sets of SAR images," *Remote Sens.*, vol. 7, no. 1, pp. 530–563, Jan. 2015.
[9] S. V. Samsonov, N. d'Oreye, P. J. González, K. F. Tiampo, L. Ertolahti, and J. J. Clague, "Rapidly accelerating subsidence in the greater vancouver region from two decades of ERS-ENVISAT-RADARSAT-2 DInSAR measurements," *Remote Sens. Environ.*, vol. 143, pp. 180–191, Mar. 2014.
[10] F. Zhao, J. Mallorqui, R. Iglesias, J. Gili, and J. Corominas, "Landslide monitoring using multi-temporal SAR interferometry with advanced persistent scatterers identification methods and super high-spatial resolution TerraSAR-X images," *Remote Sens.*, vol. 10, no. 6, p. 921, Jun. 2018.
[11] J. Liu *et al.*, "Underground coal fires identification and monitoring using time-series InSAR with persistent and distributed scatterers: A case study of Miquan coal fire zone in Xinjiang, China," *IEEE Access*, vol. 7, pp. 164492–164506, 2019.
[12] R. Zhao, Z.-W. Li, G.-C. Feng, Q.-J. Wang, and J. Hu, "Monitoring surface deformation over permafrost with an improved SBAS-InSAR algorithm: With emphasis on climatic factors modeling," *Remote Sens. Environ.*, vol. 184, pp. 276–287, Oct. 2016.
[13] H. A. Zebker and J. Villasenor, "Decorrelation in interferometric radar echoes," *IEEE Trans. Geosci. Remote Sens.*, vol. 30, no. 5, pp. 950–959, Sep. 1992.
[14] A. Ferretti, A. Fumagalli, F. Novali, C. Prati, F. Rocca, and A. Rucci, "A new algorithm for processing interferometric data-stacks: SqueeSAR," *IEEE Trans. Geosci. Remote Sens.*, vol. 49, no. 9, pp. 3460–3470, Sep. 2011.
[15] Y. Wang, X. X. Zhu, and R. Bamler, "Retrieval of phase history parameters from distributed scatterers in urban areas using very high resolution SAR data," *ISPRS J. Photogramm. Remote Sens.*, vol. 73, pp. 89–99, Sep. 2012.
[16] G. Fornaro, S. Verde, D. Reale, and A. Pauciullo, "CAESAR: An approach based on covariance matrix decomposition to improve multibaseline–multitemporal interferometric SAR processing," *IEEE Trans. Geosci. Remote Sens.*, vol. 53, no. 4, pp. 2050–2065, Apr. 2015.
[17] M. Jiang, X. Ding, R. F. Hanssen, R. Malhotra, and L. Chang, "Fast statistically homogeneous pixel selection for covariance matrix estimation for multitemporal InSAR," *IEEE Trans. Geosci. Remote Sens.*, vol. 53, no. 3, pp. 1213–1224, Mar. 2015.
[18] N. Cao, H. Lee, and H. C. Jung, "A phase-decomposition-based PSInSAR processing method," *IEEE Trans. Geosci. Remote Sens.*, vol. 54, no. 2, pp. 1074–1090, Feb. 2016.
[19] S. R. Cloude and K. P. Papathanassiou, "Polarimetric SAR interferometry," *IEEE Trans. Geosci. Remote Sens.*, vol. 36, no. 5, pp. 1551–1565, Sep. 1998.
[20] J.-S. Lee and E. Pottier, *Polarimetric Radar Imaging: From Basics to Applications*. Boca Raton, FL, USA: CRC Press, 2009.
[21] L. Pipia *et al.*, "Polarimetric differential SAR interferometry: First results with ground-based measurements," *IEEE Geosci. Remote Sens. Lett.*, vol. 6, no. 1, pp. 167–171, Jan. 2009.
[22] V. D. Navarro-Sanchez, J. M. Lopez-Sanchez, and F. Vicente-Guijalba, "A contribution of polarimetry to satellite differential SAR interferometry: Increasing the number of pixel candidates," *IEEE Geosci. Remote Sens. Lett.*, vol. 7, no. 2, pp. 276–280, Apr. 2010.
[23] V. D. Navarro-Sanchez and J. M. Lopez-Sanchez, "Improvement of persistent-scatterer interferometry performance by means of a polarimetric optimization," *IEEE Geosci. Remote Sens. Lett.*, vol. 9, no. 4, pp. 609–613, Jul. 2012.
[24] V. D. Navarro-Sanchez, J. M. Lopez-Sanchez, and L. Ferro-Famil, "Polarimetric approaches for persistent scatterers interferometry," *IEEE Trans. Geosci. Remote Sens.*, vol. 52, no. 3, pp. 1667–1676, Mar. 2014.
[25] R. Iglesias, D. Monells, X. Fabregas, J. J. Mallorqui, A. Aguasca, and C. Lopez-Martinez, "Phase quality optimization in polarimetric differential SAR interferometry," *IEEE Trans. Geosci. Remote Sens.*, vol. 52, no. 5, pp. 2875–2888, May 2014.
[26] V. D. Navarro-Sanchez and J. M. Lopez-Sanchez, "Spatial adaptive speckle filtering driven by temporal polarimetric statistics and its application to PSI," *IEEE Trans. Geosci. Remote Sens.*, vol. 52, no. 8, pp. 4548–4557, Aug. 2014.
[27] R. Iglesias, D. Monells, C. Lopez-Martinez, J. J. Mallorqui, X. Fabregas, and A. Aguasca, "Polarimetric optimization of temporal sublook coherence for DInSAR applications," *IEEE Geosci. Remote Sens. Lett.*, vol. 12, no. 1, pp. 87–91, Jan. 2015.
[28] M. Esmaeili and M. Motagh, "Improved persistent scatterer analysis using amplitude dispersion index optimization of dual polarimetry data," *ISPRS J. Photogramm. Remote Sens.*, vol. 117, pp. 108–114, Jul. 2016.

[29] A. G. Mullissa, D. Perissin, V. A. Tolpekin, and A. Stein, "Polarimetry-based distributed scatterer processing method for PSI applications," *IEEE Trans. Geosci. Remote Sens.*, vol. 56, no. 6, pp. 3371–3382, Jun. 2018.
[30] Z. Sadeghi, M. J. Valadan Zoej, A. Hooper, and J. M. Lopez-Sanchez, "A new polarimetric persistent scatterer interferometry method using temporal coherence optimization," *IEEE Trans. Geosci. Remote Sens.*, vol. 56, no. 11, pp. 6547–6555, Nov. 2018.
[31] F. Zhao and J. J. Mallorqui, "Coherency matrix decomposition-based polarimetric persistent scatterer interferometry," *IEEE Trans. Geosci. Remote Sens.*, vol. 57, no. 10, pp. 7819–7831, Oct. 2019.
[32] F. Zhao and J. J. Mallorqui, "SMF-POLOPT: An adaptive multitemporal Pol(DIn)SAR filtering and phase optimization algorithm for PSI applications," *IEEE Trans. Geosci. Remote Sens.*, vol. 57, no. 9, pp. 7135–7147, Sep. 2019.
[33] M. Neumann, L. Ferro-Famil, and A. Reigber, "Multibaseline polarimetric SAR interferometry coherence optimization," *IEEE Geosci. Remote Sens. Lett.*, vol. 5, no. 1, pp. 93–97, Jan. 2008.
[34] A. Mestre-Quereda, J. M. Lopez-Sanchez, J. D. Ballester-Berman, P. J. Gonzalez, A. Hooper, and T. J. Wright, "Evaluation of the multilook size in polarimetric optimization of differential SAR interferograms," *IEEE Geosci. Remote Sens. Lett.*, vol. 15, no. 9, pp. 1407–1411, Sep. 2018.

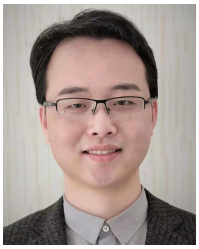

Feng Zhao (Member, IEEE) received the M.S. degree from the China University of Mining and Technology (CUMT), Xuzhou, China, in June 2016, and the Ph.D. degree from the Universitat Politècnica de Catalunya, Barcelona, Spain, in September 2019.

Since November 2019, he has been with the School of Environment Science and Spatial Informatics, CUMT, and with the Key Laboratory of Land Environment and Disaster Monitoring of the Ministry of Natural Resources of China, as an Assistant Professor. His main work focuses on the development of advanced pixel selection and optimization algorithms for multitemporal (Pol)DInSAR techniques. His research interests include advanced multitemporal InSAR techniques and their application in terrain deformation detection and disaster monitoring.

Jordi J. Mallorqui (Senior Member, IEEE) was born in Tarragona, Spain, in 1966. He received the Ingeniero degree in telecommunications engineering and the Doctor Ingeniero degree in telecommunications engineering for his research on microwave tomography for biomedical applications with the Department of Signal Theory and Communications, Universitat Politècnica de Catalunya (UPC), Barcelona, Spain, in 1990 and 1995, respectively.

Since 1993, he has been teaching the School of Telecommunications Engineering of Barcelona, UPC, first as an Assistant Professor, later in 1997, as an Associate Professor, and since 2011, as a Full Professor. He has been the Head of the Department of Signal Theory and Communications since October 2017. His teaching activity involves microwaves, radio navigation systems, and remote sensing. He spent a sabbatical year with Jet Propulsion Laboratory, Pasadena, CA, USA, in 1999, working on interferometric airborne synthetic aperture radar (SAR) calibration algorithms. He is working on the application of SAR interferometry to terrain deformation monitoring with orbital, airborne, and ground data; vessel detection and classification from SAR images; and 3-D electromagnetic (EM) simulation of SAR systems. He is also collaborating in the design and exploitation of small SAR interferometers onboard UAVs for subsidence and landslide control and SAR systems for autonomous vehicles. He holds one patent and has published more than 200 articles in refereed journals and international symposia.

Dr. Mallorqui has been a member of the Scientific Committee of several international symposia. He has served as an Associate Editor for the IEEE TRANSACTIONS ON GEOSCIENCE AND REMOTE SENSING and a Guest Editor for *Journal of Applied Geophysics*.

Juan M. Lopez-Sanchez (Senior Member, IEEE) was born in Alicante, Spain, in 1972. He received the Ingeniero (M.S.) and Doctor Ingeniero (Ph.D.) degrees in telecommunication engineering from the Technical University of Valencia, Valencia, Spain, in 1996 and 2000, respectively.

From 1998 to 1999, he was a Pre-Doctoral Grant Holder with the Space Applications Institute, Joint Research Center of the European Commission, Ispra, Italy. Since 2000, he has been the Leader of the Signals, Systems and Telecommunication Group, University of Alicante, Alicante, where he has also been a Full Professor since 2011. He has coauthored more than 80 articles in refereed journals and more than 130 articles and presentations in international conferences and symposia. His research interests include microwave remote sensing for inversion of biophysical parameters, polarimetric and interferometric techniques, synthetic aperture radar imaging algorithms, and applications of radar remote sensing in agriculture and geophysics.

Dr. Lopez-Sanchez received the 2001 Indra Award for the best Ph.D. thesis about radar in Spain. From 2006 to 2012, he was the Chair of the Spanish Chapter of the IEEE Geoscience and Remote Sensing Society.